Nuclear Materials and Energy 20 (2019) 100698

Contents lists available at ScienceDirect

Nuclear Materials and Energy

journal homepage: www.elsevier.com/locate/nme

Study of the microstructure and small punch behavior of a 9Cr ODS tube

Elvira Oñorbe[a,*], Mercedes Hernández-Mayoral[a], Alasdair Morrison[b], Marta Serrano[a]

[a] Division of Energy Interest Materials/CIEMAT. Madrid Spain
[b] Department of Materials/University of Oxford. United Kingdom

ARTICLE INFO

Keywords:
ODS steels
Small punch
Deformation mechanisms
Electron microscopy

ABSTRACT

The microstructure of a 9Cr ODS tube (supplied by CEA) obtained by a powder metallurgy route followed by hot extrusion and cold pilgering of the final cladding, has been investigated by means of scanning and transmission electron microscopy. The alloy presents a weak fiber texture and a bimodal grain size distribution. Three different families of precipitates have been identified: isolated and large Ti-Al oxides, Cr rich precipitates placed preferentially at prior austenite grain boundaries and martensitic lath boundaries and a fine distribution of Y-Ti nano-oxides within grains. In order to correlate this microstructure with the mechanical properties, 3 mm diameter discs drilled from the tube wall were tested by small punch technique at room temperature, 300 °C and 500 °C to reproduce the load system to which the claddings will be subjected under service conditions. Changes in the slip character and failure mode as temperature increases were observed. At low temperatures the alloy exhibited a wavy slip character and a quasi-ductile fracture mode. At high temperature, 500 °C, the fracture tended to be more brittle, what may be attributed to an intergranular deformation mechanism leading to the weakening of grain boundaries.

1. Introduction

Ferritic/martensitic oxide dispersion strengthened (F/M ODS) steels have been considered an alternative to austenitic steels for cladding application in the sodium fast reactors (SFR) for generation IV program. Since F/M steels have shown good irradiation behavior such as low void swelling, with regard to mechanical properties, their creep strength at high temperature, above 650 °C, is not good enough for fuel pin applications [1,2]. A way to improve high temperature mechanical behavior and the radiation resistance of F/M steels can be conducted by inserting a fine dispersion of hard nano-oxide particles in the matrix, making them good candidates for cladding material in Generation IV nuclear reactors [3–7]. These nano-oxide particles enhance mechanical properties at high temperature as they act as effective barriers to dislocation motion, holding deformation and limiting grain growth. Concerning radiation resistance, nano-oxide particles act as a sink for irradiation induced defects [1,8].

The fabrication route of ODS materials for fast reactor fuel cladding applications is critical. Extrusion and cold rolling processes normally lead to elongated grains parallel to the deformation direction that are detrimental for mechanical properties under hoop stress to which the cladding will be subjected under service conditions [9–11]. Extensive research into the use of intermediate heat treatments allows controlling the final microstructure, which is strongly linked to the chemical composition of the alloy. Thus, in the case of 9Cr ODS tube, reversible phase transformation from ferrite-martensite to austenite during heat treatments, leads to a reduction of the crystallographic and morphologic anisotropy [12–15].

The aim of this work is to analyze the microstructure of a 9Cr ODS tube supplied by CEA within the European Union funded MatISSE project [16] and correlate the mechanical properties estimated by small punch tests at room temperature (RT), 300 °C and 500 °C. Finally, the analysis of the tested sample surfaces will help to elucidate the possible slip character and failure mechanisms at different temperatures.

2. Materials and methods

The tested material was a 9Cr ODS (CEA code: K49) tube supplied by CEA within the MatISSE project. The cladding was obtained by a powder metallurgy route where the master alloy was mechanically alloyed with 0.3 wt% Y_2O_3 under a hydrogen atmosphere in a vertical attritor mill. The raw tube was obtained by hot extrusion at 1100 °C, and finally the cladding was cold formed by a sequence of High Pressure Tube Reducer (HPTR) cold pilgering rolling passes [17] with

* Corresponding author.
E-mail addresses: elvira.onorbe@ciemat.es (E. Oñorbe), m.mayoral@ciemat.es (M. Hernández-Mayoral), alasdair.morrison@materials.ox.ac.uk (A. Morrison), marta.serrano@ciemat.es (M. Serrano).

https://doi.org/10.1016/j.nme.2019.100698
Received 1 March 2019; Received in revised form 21 June 2019; Accepted 28 July 2019
Available online 30 July 2019

Table 1
Chemical composition (wt.%).

	Cr	Ni	Si	W	Mn	Ti	C	N	O	Y
K49	9.1	0.20	0.23	1.05	0.29	0.20	0.109	0.022	0.12	0.19

intermediate heat treatments performed in the austenitic domain at 1050 °C followed by slow cooling to reduce stresses, obtaining cladding tubes with 10.73 mm outer diameter and 0.5 mm wall thickness. The final heat treatment was a normalization at 1050 °C followed by tempering at 750 °C for 1 h [18]. The final composition of the tube is given in Table 1.

The microstructure of the as received tube was analysed using Scanning Electron Microscopy/Electron Back Scattered Diffraction (SEM/EBSD) in the longitudinal direction using Channel 5 EBSD software on a Hitachi SU6600 field emission gun scanning electron microscope (FEG-SEM) equipped with an Oxford Instruments HKL Nordlys detector. The samples analysed were 3 mm discs drilled from the tube wall and polished up to the desire thickness of 0.1 mm with a final electrolytic polishing with 5% perchloric acid and methanol at −60 °C as surface preparation method. The small size of the sample allows reduction of the amount of ferromagnetic material, which decreased sample drift during measurements. The initial microstructure was also studied by transmission electron microscopy (TEM), on specimens prepared by electrolytic polishing using a mixture of 5% perchloric acid and methanol at −60 °C. TEM analysis was carried out using standard imaging methods of Bright Field (BF) and Weak Beam Dark Field (WBDF) in a TEM JEOL JEM-2010 with LaB_6 filament operating at 200 keV available at CIEMAT. Furthermore, Energy-Filtered Transmission Electron Microscopy (EFTEM) was employed to obtain nanometer resolution chemical maps using the JEOL 2200 MCO field emission gun TEM/STEM available at the Department of Materials of the University of Oxford. The microscope and its capabilities are described in [19]. For EFTEM analysis, thin lamellas of the material were prepared by focused ion beam (FIB) in the same department using a Zeiss NVision FIB-SEM microscope. Multivariate statistical analysis (MSA) was applied to the dataset to produce a ``noise-free" reconstruction [19].

Grain size was estimated by image analysis techniques based on EBSD maps. In order to use this method it was necessary to define grains drawing the border between high and low angle boundaries and set the input values for the EBSD post-processing software. In the case of ODS tubes, after processing there was a large amount of stored energy within grains in the form of highly deformed microstructure leading to a wide range of misorientation angles that were analysed to establish the border between low and high angle grain boundaries (HAGBs). Following this method, HAGBs were considered above 10° misorientation angle between two grains. The results were adjusted to a LogNormal function to estimate the mean grain size value. Size and distribution of the different families of precipitates found in the alloy were measured using SEM images for the larger ones and TEM images for the nano-particles employing JMicroVision software [20]. In the latter, more than 1500 precipitates were measured in 20 images being the total analysed volume 6.2×10^7 nm^3. Number density was obtained by counting precipitates in the TEM images and divided by the analysed volume. Thickness measurements were done employing Convergent Beam Electron Diffraction (CBED) method [21]. Finally, Energy Dispersive Spectroscopy (EDS) for TEM was used to analyse the composition of the precipitates present in the alloy.

Small punch (SP) tests were used as a screening method to evaluate the mechanical behavior of 9Cr ODS tube. In addition, these type of tests can reproduce the biaxial stress mode the cladding will be subjected to under service conditions. 3 mm diameter curved specimens were drilled from the 9Cr ODS wall tube with 0.50 mm thickness. Plane-parallel specimens were obtained by polishing both sides of the 3 mm discs until 0.250 mm thickness was reached. The tests were carried out in the small punch testing machine designed and available at CIEMAT at a displacement rate of 0.3 mm/min at RT, 300 °C and 500 °C, using a punch of 1 mm diameter. Two specimens were tested per each temperature condition.

In the case of small punch tests, the results are not directly comparable with those obtained with traditional uniaxial tests due to the transient stress state. The test result is a load vs deflection (displacement) curve where the main parameters of the curve are described in the European Code of Practice for Small Punch Testing for Tensile and Fracture Behaviour [22]:

- P_m [N] – maximum load recorded during SP test,
- P_y [N] – load characterizing the transition from linearity to the stage associated with the spread of the yield zone through the specimen thickness (plastic bending stage),
- d_m [mm] – displacement corresponding to maximum load m F,
- E^{SP} [J] – SP fracture energy obtained from the area under the load punch displacement curve up to maximum load.

3. Results

3.1. Microstructure

Fig. 1(a) shows the SEM image of the 9Cr ODS tube in the longitudinal direction (LD). A distribution of Cr rich carbides (identified by EDS analysis), decorating prior austenite grain boundaries and packet boundaries (dash white arrow in Fig. 1(b)) were visible. Most of them have a polygonal shape and the size distribution was estimated and adjusted to a LogNormal function with mean value 90 ± 1 nm (Fig. 1(c)) ranging from a few dozens of nanometers to more than a half micron. The volume fraction was measured in the same images and corresponds to a 3% of the total volume of the alloy. Isolated Ti-Al oxides (identified by EDS analysis) occasionally nucleated either at grain boundaries or within grains with sizes ranging between 500 nm and 2 μm were visible. The Al present in the alloy comes from contamination during the milling process as has been previously reported [23]. At higher magnification (Fig. 1(b)) smaller Cr rich carbides that nucleated at lath grain boundaries (white arrow) were observed with sizes ranging from 20 nm up to 100 nm measured along the long axis.

Fig. 2(a) shows an inverse pole figure (IPF) map of the 9Cr ODS tube in the longitudinal direction. The alloy had an almost random grain orientation distribution (weak texture) and a bimodal grain size of coarse and deformed grains together with regions of small and recrystallized grains in between (white circles in Fig. 2(a)) occupying 19.8% of the total area measured (9.5×10^3 μm^2). A diagram of the misorientation angle and grain size distribution is presented in Fig. 2(b) and Fig. 2(c), respectively. Those with a misorientation above 10° have been considered HAGBs, and included in the grain size analysis. Grain size analysis was completed considering two distinct families: coarse and deformed grains ranging from 1 to 10 μm; and small grain regions, where the grain size ranged from 100 nm to 1 μm. Those boundaries with a misorientation between 2° and 10° have been considered low angle grain boundaries (LAGBs) and the bulk of them were concentrated from 2° to 5°.

Fig. 3(a) and (b) shows the microstructure of the 9Cr ODS tube examined by TEM. As per the SEM analysis, a grain structure of packets of martensitic laths and a small number of ferritic subgrains within prior austenite grains were visible. Dense networks of dislocations were present within grains, an indication of the internal stresses induced by the fabrication process. A fine dispersion of nano-oxides was observed within the matrix (Fig. 3(c)). The fine microstructural observations showed that the dislocations were pinned at several points (white arrows in Fig. 3(c)). The size distribution of the nano-oxides was measured and the results adjusted to a LogNormal distribution (Fig. 3(d)). A wide distribution ranging from 1.5 up to 20 nm was obtained being the

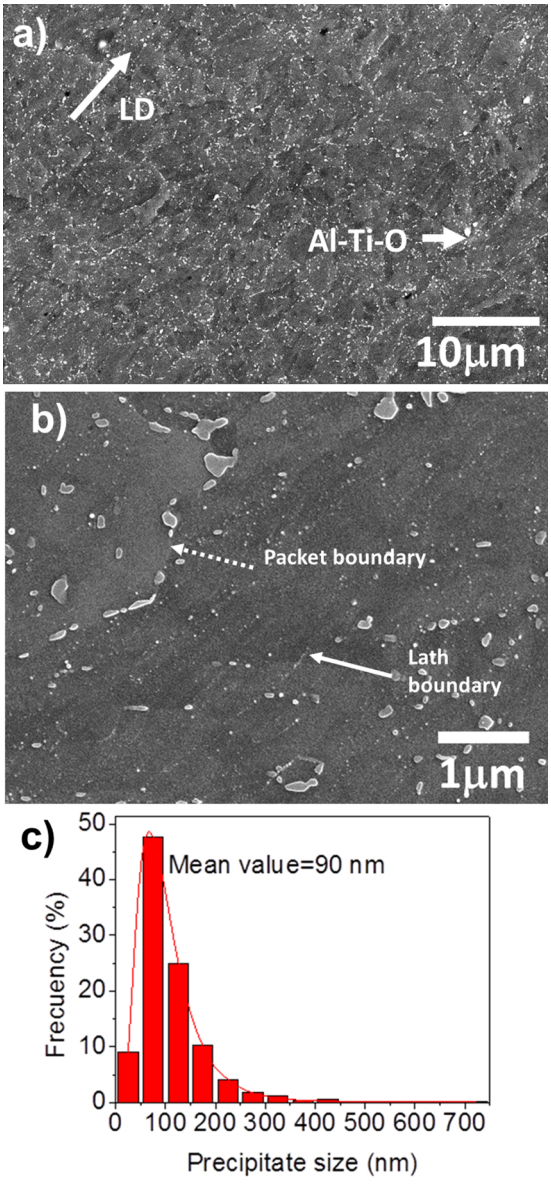

Fig. 1. (a) SEM image of 9CrODS tube in the longitudinal direction, (b) microstructure after processing: packets with martensitic laths within prior austenitic grains and (c) precipitate size distribution.

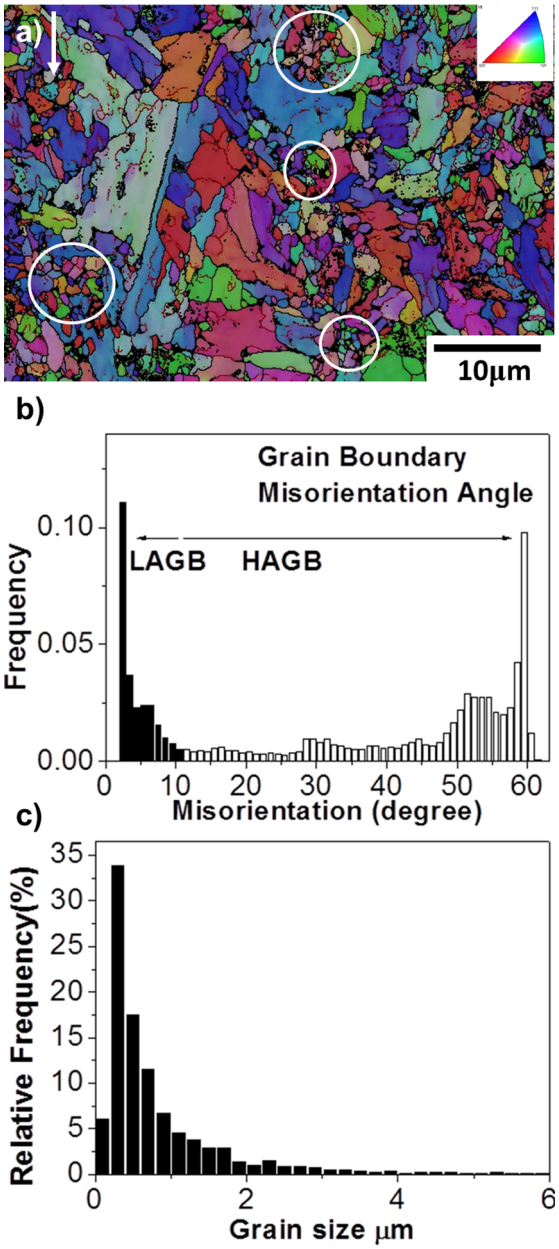

Fig. 2. (a) IPF map of 9CrODS tube in the longitudinal direction, (b) grain boundary misorientation angle and (c) grain size distribution.

mean value (4 ± 1) nm. The same regions were used to estimate the nano-oxide number density, obtaining a value of (1.3 ± 0.2) × 10^{23} particle/m^3.

EDS was used to analyse the composition of the precipitates and nano-oxides present in the alloy. The results shown in Fig. 4(a)–(c) indicated the presence of three distinct families according to size and composition. The larger precipitates (500 nm up to ~2 μm) were confirmed as Ti-Al oxides (Fig. 4(a)). Ti-Al oxides are isolated and formed either in the matrix and/or at grain boundaries. The second family of precipitates were Cr rich carbides (Fig. 4(b)) preferentially located at prior austenite grain boundaries and also found intra-laths with sizes ranging from 20 to 500 nm. Finally, the finest precipitates were identified as nano-oxides, with a mean size value of 4 nm, composed of O, Ti and Y (Fig. 4(c)). The analysis of at least 20 nano-oxides was used to calculate the Y/Ti ratio, obtaining values ranging from 0.5 to 1.8. This results are plotted in Fig. 4(d) where Y/Ti ratio increases up to saturation around 1.4 as particle size increase up to 15 nm.

Low-loss (10–80 eV) EFTEM maps are presented in Fig. 5 following MSA ``noise free" reconstruction. Some nano-oxides with sizes ranging from 2 nm up to 12 nm were analyzed, showing, in the case of the larger particle (12 nm), a Y-Ti rich core with a shell of ~2 nm enriched in Cr and a decrease of the Fe signal compared with the one from the matrix that has been previously reported in other ODS materials [24–26]. In the large, 12 nm, particle the Ti demonstrated local intensity variation, with significant difference between the core and the shell. Y and Ti were co-located in some particles, though the finest particles were again confirmed to have a higher Y fraction.

3.2. Small punch tests results

The load vs the displacement results for the small punch test for the 9Cr ODS tube at room temperature, 300 °C, and 500 °C are given in Fig. 6. The curve morphologies are similar for the different samples. A decrease in the small punch energy (E^{SP}), measured as the area under the curve, was visible as the test temperature increased indicating a decrease in the ductility of the material according to CWA 15627 [22].

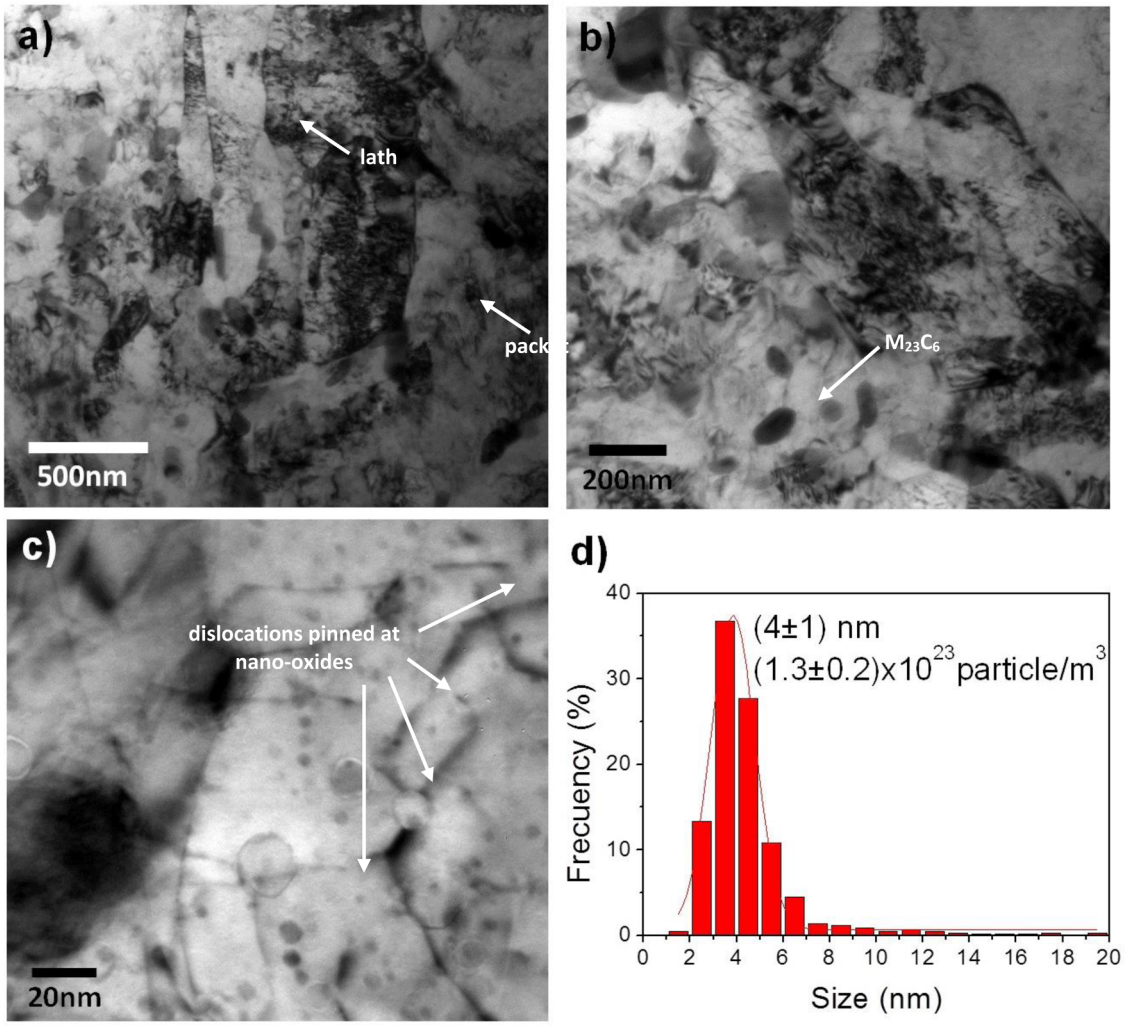

Fig. 3. (a) TEM bright field images of 9CrODS tube where martensitic laths and (b) ferritic grains are visible. (c) A detail of the dislocation-nano-oxides interaction and (d) nano-oxide particle size distribution.

Also, the alloy tested at 500 °C showed the weakest response to deformation with a maximum load around 280 N.

The maximum load (P_m) and yield strength (P_y) dependence with temperature has also been represented in Fig. 7(a) and (b) respectively. P_m decreased slightly from 500 N to 280 N as temperature increased, whilst P_y was similar at RT and 300 °C, around 80 N, only decreasing at 500 °C to 50 N, suggesting a change in the yielding mechanism at the higher test temperature.

The SEM analysis of the surface of the deformed small punch specimens was carried out to provide new tools to better understand the failure mechanisms at the different temperatures. The tested samples for the three different temperatures are shown in Fig. 8. At room temperature, a circumferential crack separates the cup from the rest of the specimen (Fig. 8(a) and (d)) which is an evidence of a ductile failure [27]. On the other hand radial cracks start to appear at 300 °C (black arrows in Fig. 8(b), and are clearly visible and more numerous at 500 °C (Fig. 8(c) and (f)) suggesting a change of the failure process from quasi-ductile fracture at low temperature to brittle fracture at high temperature. Slip bands are visible at higher magnification in all the surfaces of the tested specimens. At RT and 300 °C a rumpling surface is observed while at 500 °C planar offsets are visible on the surface. Overall, Fig. 8 and the results of small punch tests presented in Figs. 6 and 7 suggest that rising temperature led to a change in the deformation and fracture behavior indicating a transition from quasi-ductile to brittle failure mode.

4. Discussion

A 9Cr ODS tube was studied after powder metallurgical processing, identifying characteristic microstructures. Small punch tests were carried out at room temperature, 300 °C, and 500 °C and the resulting deformed surfaces of tested specimens studied, giving evidence of a change in the deformation mechanisms in operation at the different temperatures.

As previously remarked, ODS fabrication routes play an essential role to obtain suitable mechanical properties. In this case, the final tempering heat treatment of 1 h duration resulted in a bcc structure with a weak texture consisting of retained martensitic lath structure and small interspersed ferritic grains. This kind of bimodal grain size structure is desirable to achieve high strength without loss of ductility [28]. Martensitic laths will contribute to hinder crack formation and/or propagation of intergranular cracks during deformation and also to enhance ductility while the small ferritic grain regions will provide high strength and hardness. Furthermore, during intermediate heat treatments, the complete transformation from ferrite to austenite takes place reducing the crystallographic and morphologic texture [15,17,29–31], which was desirable to reduce grain boundary sliding among elongated grains during deformation.

Besides the final grain microstructure, the precipitates present in the alloy play an important role in the evolution of the microstructure and the mechanical properties of the material. Different families were

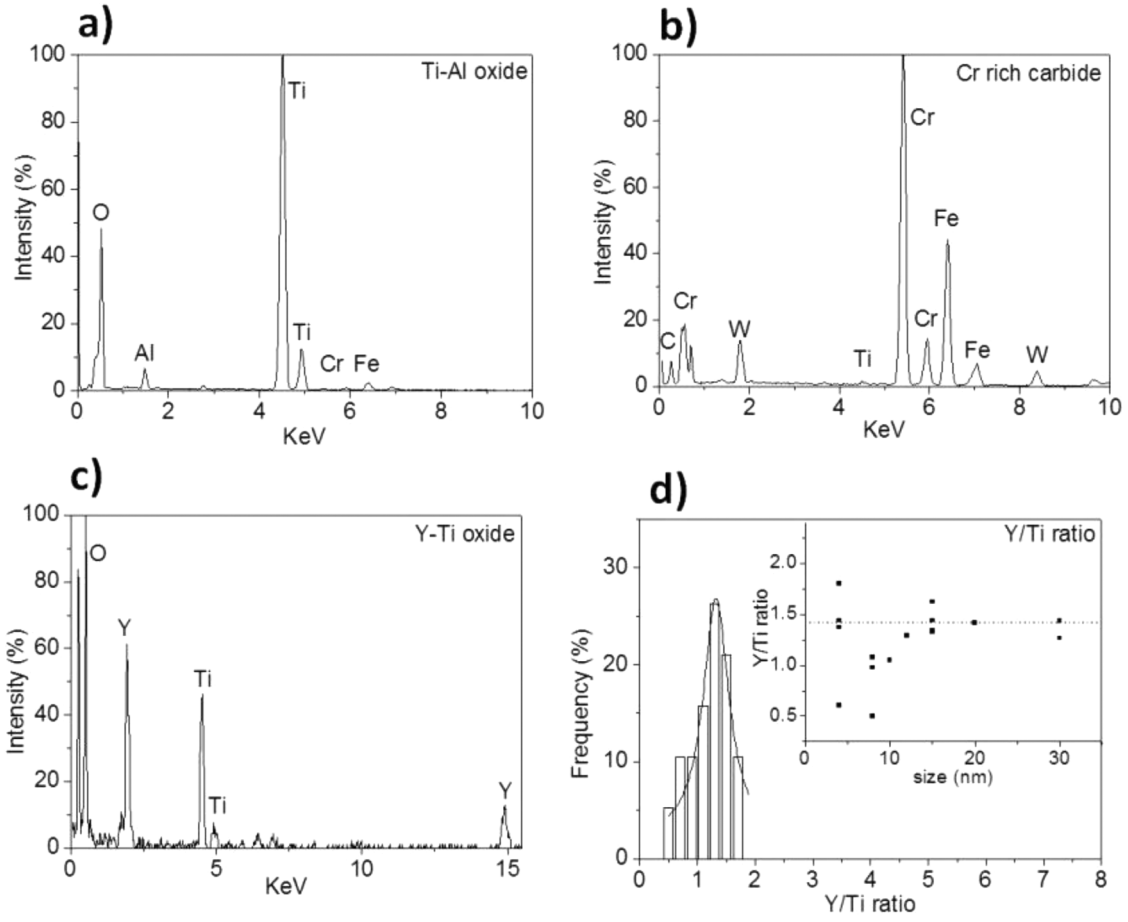

Fig. 4. EDX analysis results: (a) Ti-Al oxide, (b) Cr rich carbide, (c) Y-Ti oxide and (d) Y/Ti ratio vs frequency and particle size.

identified during microstructural analysis. The coarser particles, larger than 500 nm, are inclusions composed mainly of Ti-Al-O, as shown Fig. 1(a). These precipitates were isolated and in a very low volume fraction, therefore it is not expected that they have a significant influence in the mechanical behavior of the material. On the contrary, a high volume fraction of Cr rich carbides (that most probably corresponds to $M_{23}C_6$ carbides, as it has been widely analyzed in literature and in accordance with the phase diagram [14,32,33]) were found to be homogeneously distributed at prior austenite grain boundaries, packets and martensitic laths boundaries. Those located at the prior austenite boundaries were the larger ones and were likely to have formed during the austenitizing heat treatment, having therefore, enough time for diffusion and growth. Other authors attribute this coarsening of the Cr rich carbides to an enhanced diffusion along the Prior Austenitic Grain Boundaries (PAGBs), increasing the coarsening rate [34–36]. These are high angle grain boundaries (HAGBs) and the diffusion rates are faster than those for low angle grain boundaries (LAGBs) such is the case of martensite lath boundaries. Carbides located within grains (Fig. 1(b)) are hypothesized to have precipitated intra-lath during tempering, with less time for growth due to slower diffusion rates associated with LAGBs, as has been explained above, resulting in them being smaller. Although these precipitates do not contribute to the dispersion hardening within grains, Cr rich carbides located at grain boundaries can play an important role in the mechanical properties at high temperature enhancing sub-boundary hardening, hindering the migration of laths and blocking grain growth and grain boundary sliding. Furthermore, those placed within grains will contribute to mechanical properties as obstacles to dislocation movements during deformation but not as efficiently as nano-oxides [37,38].

Finally, a homogeneous distribution of nano-oxides particles and a high interaction with dislocations was observed within grains, which is the principal responsible of the dispersion hardening of the material and contributes to sub-grain hardening stabilizing laths boundaries [34]. The size and distribution of nano-oxide particles are key factors in the evolution of the microstructure and hence the mechanical properties during deformation. In our case a fine dispersion of nano-oxides was observed with a mean size value of 4 nm, in accordance with the results obtained by Toualbi et al. [18]. The Y/Ti ratio estimated allows knowing the stoichiometry of the particles according with Sakasegawa et al. [39] who observed that this ratio increased with increasing particle sizes up to a saturation value of 1.4 for stoichiometric $Y_2Ti_2O_7$ composition. This value is achieved when the particle size is above around 15 nm. Below this size, these particles are non-stoichiometric and the Y/Ti ratio is <1.

The consequences of this microstructure were a particular mechanical behavior. Small punch results shown that the key change in the mechanical response takes place as test temperature increases, especially in the case of yield strength drop between 300 °C and 500 °C. Understanding of the previous microstructure and analysis of the fracture samples after small punch tests provided the necessary information to identify the slip character and the possible fracture and deformation mechanisms that could be operating at different temperature ranges and explain this behavior.

First of all the presence of a fine dispersion of nano-oxides within the matrix and a high interaction with dislocations can provide insights of what happens during deformation. It is well known that the deformation mechanisms in ODS material are controlled by the interaction of dislocation with the obstacles present in the matrix. At room temperature the main features observed for the 9Cr ODS tube are clearly slip lines and a surface rumpling, indicating that there is a

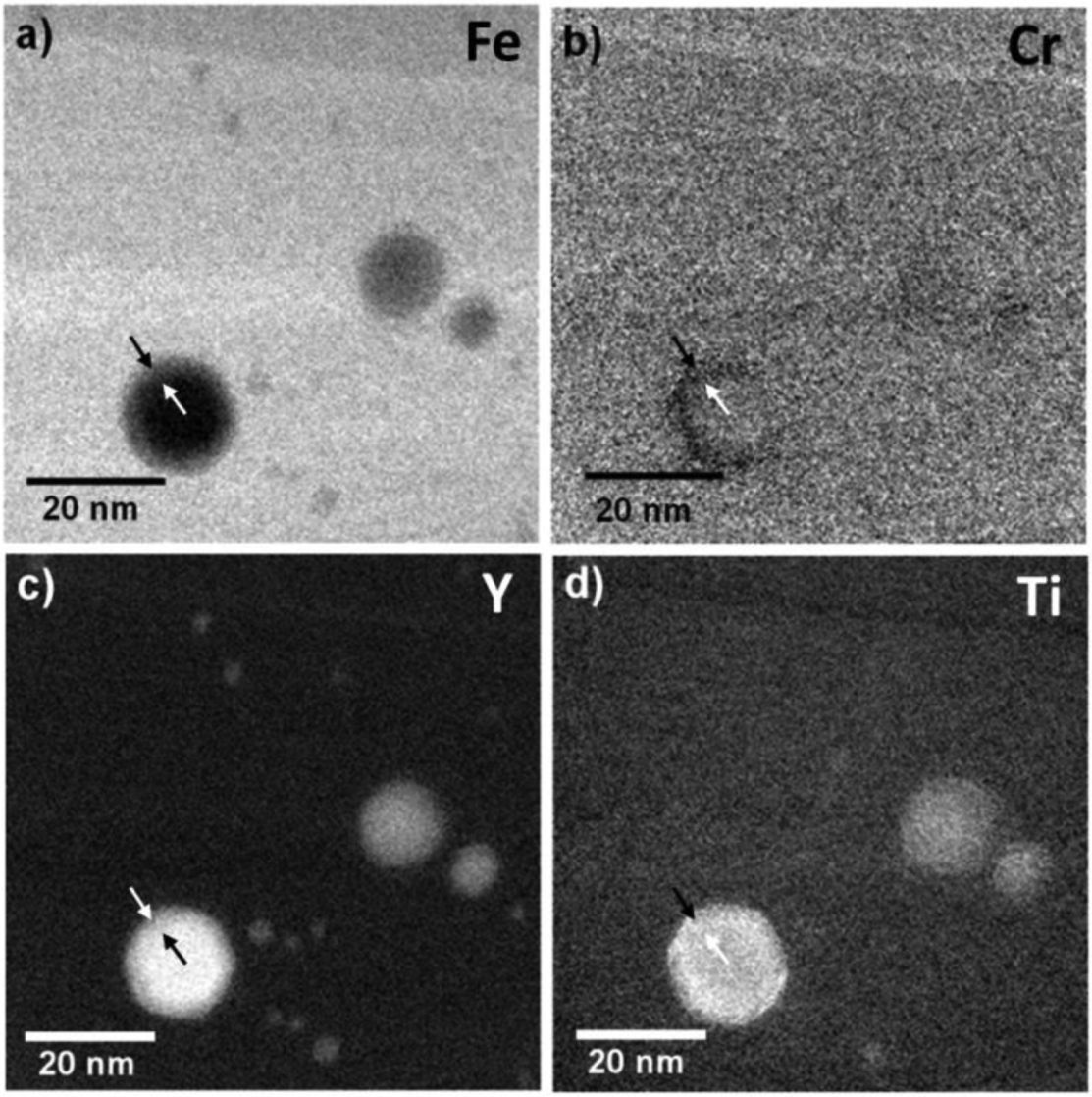

Fig. 5. EFTEM elemental maps after MSA "noise-free" reconstruction from the low-loss dataset: (a) matrix (Fe $M_{2,3}$), (b) Cr $M_{2,3}$, (c) Y $N_{2,3}$, and (d) Ti $M_{2,3}$.

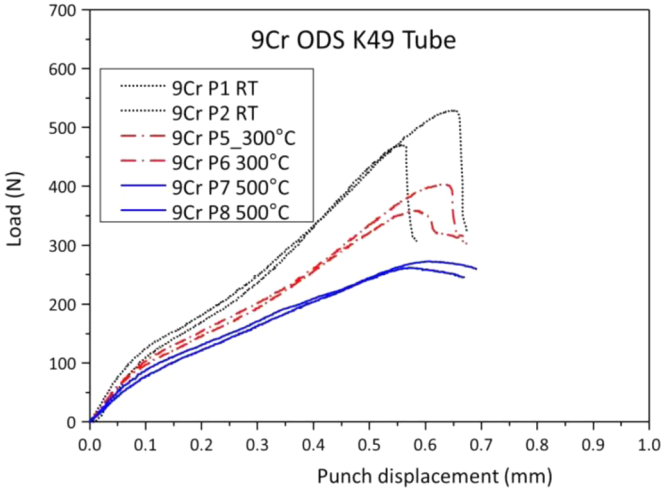

Fig. 6. Load vs displacement curves at RT, 300 °C, and 500 °C for 9CrODS tube. P1, P2, P5, P6, P7 and P8 correspond to the different small punch tests carried out.

homogeneous deformation of the material. This was in agreement with the fine dispersion of nano-oxides in the as-received material shown in Fig. 3(a). During deformation dislocations are pinned at nano-oxides and cannot reach grain boundaries. Additionally, macro-crack appearance agrees with a ductile failure mode, with a circumferential crack propagation path [40].

As temperature increases thermal activated mechanisms can start to operate, dislocations can move easily to lath and block boundaries, overpass obstacles reaching and accumulating at grain boundaries and weakening them as was suggested by Praud et al. after in situ TEM deformation experiments [41]. At some point the stress arising at grain boundaries reach a value that leads to an intergranular fracture. This is in accordance with the SEM analysis of the deformed samples at 500 °C. Planar shear offsets were visible on surfaces, indicating that dislocations remain in planar arrays. Furthermore, radial cracks start to appear in the tested disc at 300 °C and are obvious at 500 °C indicating less ductile fracture at 500 °C than at 300 °C, in close agreement to the loss of ductility and changes in the fracture behavior as observed elsewhere in ODS steels at high temperature [36,41,42]. At 500 °C cracks may initiate more readily and propagation is along grain boundaries due to

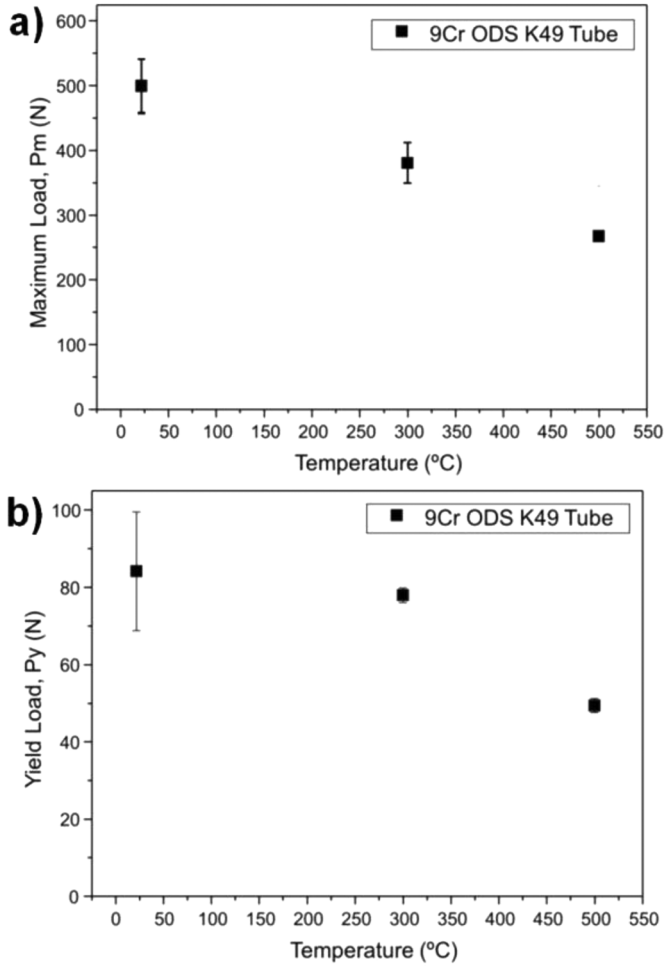

Fig. 7. (a) Maximum load vs temperature and (b) Yield strength vs temperature for 9CrODS tube.

the growth and coalescence of microcavities. This embrittlement at high temperature leads to a reduction of the yield strength and maximum load observed in Fig. 7(a) and (b).

In this sense, the change of the crack patterns observed for the three specimens, RT, 300 °C and 500 °C can be associated to a change of the fracture mechanisms from quasi-ductile and wavy slip character at RT towards a brittle intergranular failure mode and planar slip character with increasing temperature. Although the failure modes may depend on the testing and hence, do not represent the likely cladding failure behavior, small punch testing has been used as screening criteria to assess temperature effects.

5. Conclusions

Microstructural and mechanical behavior analysis by means of SEM/EBSD, TEM and small punch testing was undertaken for a 9Cr ODS tube. The main points that may be drawn are:

- The 9Cr ODS tube studied in this work presents a bimodal grain size distribution and a weak texture desirable to hinder grain boundary sliding during deformation at high temperature.
- A homogeneous distribution of Cr rich precipitates was identified at prior austenite and martensitic boundaries as well as a fine dispersion of Y-Ti nano-oxides within grains responsible for the dispersion hardening of the alloy.
- Small punch has been successfully used to assess temperature effects. Results suggest a change in the mechanical behavior with increasing temperature. At 500 °C there is a drop in the small punch energy showing decreasing ductility.
- There is a change from quasi-ductile and a wavy slip character at RT, where dislocations are pinned at nano-oxides and cannot reach grain boundaries, to a brittle failure mode and a planar slip character as temperature increases due to the activation of new deformation modes, reducing the energy requirement for dislocations to overpass obstacles and accumulate at grain boundaries.

Declaration of Competing Interest

The authors declare that they have no known competing financial interests or personal relationships that could have appeared to influence the work reported in this paper.

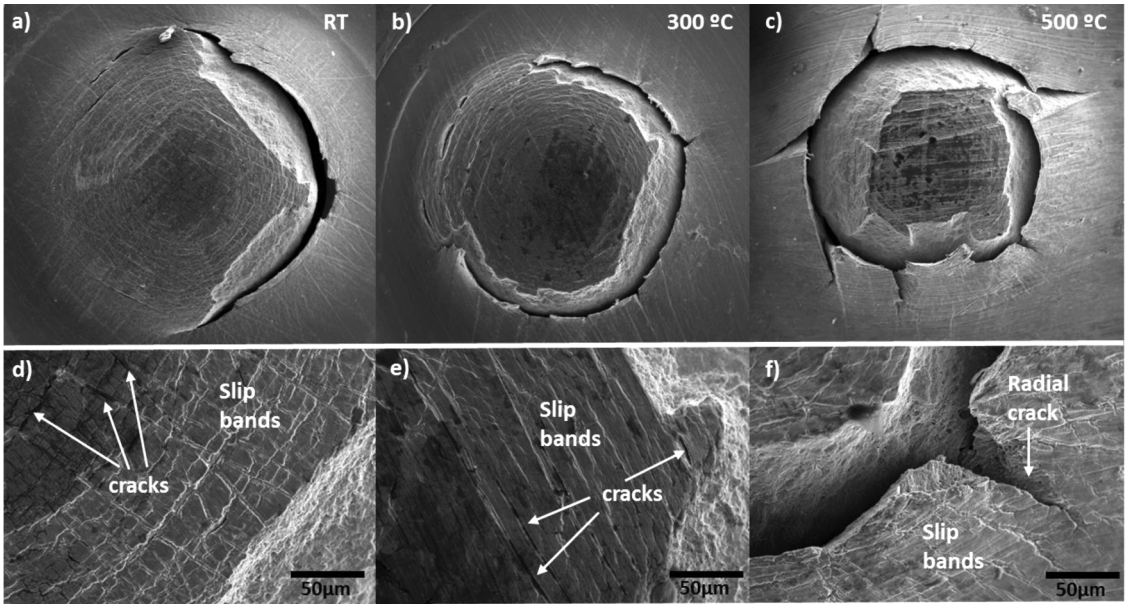

Fig. 8. SEM images of small punch fracture for 9CrODS tube at (a), (d) RT, (b), (e) 300 °C and (c), (f) 500 °C.

Acknowledgements

Part of this work is supported by the European Commission under the FP7 MatISSE project, Grant Agreement n.604862, the ESTEEM2 project (n.312483) and in the framework of the EERA (European Energy Research Alliance) Joint Program on Nuclear Materials as well as the National projects FERROGENESYS (Mat2013-47460) and FERRONESS (Mat2016-80875). E. Oñorbe would also like to thank José Castillejo grant (CAS15/00290). The authors want to acknowledge also to Mr. M. González-Castaño for TEM sample preparation and Mr. D. Plaza for carrying out the small punch tests.

Supplementary materials

Supplementary material associated with this article can be found, in the online version, at doi:10.1016/j.nme.2019.100698.

References

[1] P. Dubuisson, Y. de Carlan, V. Garat, M. Blat, ODS ferritic/martensitic alloys for sodium fast reactor fuel pin cladding, J. Nucl. Mater. 428 (2012) 6–12 https://doi.org/10.1016/j.jnucmat.2011.10.037.

[2] J.S. Cheon, C.B. Lee, B.O. Lee, J.P. Raison, T. Mizuno, F. Delage, J. Carmack, Sodium fast reactor evaluation: core materials, J. Nucl. Mater. 392 (2009) 324–330 https://doi.org/10.1016/j.jnucmat.2009.03.021.

[3] S. Ukai, M. Harada, H. Okada, M. Inoue, S. Nomura, S. Shikakura, K. Asabe, T. Nishida, M. Fujiwara, Alloying design of oxide dispersion strengthened ferritic steel for long life FBRs core materials, J. Nucl. Mater. 204 (1993) 65–73 https://doi.org/10.1016/0022-3115(93)90200-I.

[4] A. Alamo, V. Lambard, X. Averty, M.H. Mathon, Assessment of ODS-14%Cr ferritic alloy for high temperature applications, J. Nucl. Mater. 329-333 (2004) 333–337 https://doi.org/10.1016/j.jnucmat.2004.05.004.

[5] R.L. Klueh, J.P. Shingledecker, R.W. Swindeman, D.T. Hoelzer, Oxide dispersion-strengthened steels: A comparison of some commercial and experimental alloys, J. Nucl. Mater. 341 (2005) 103–114 https://doi.org/10.1016/j.jnucmat.2005.01.017.

[6] R. Lindau, A. Möslang, M. Rieth, M. Klimiankou, E. Materna-Morris, A. Alamo, A.-A.F. Tavassoli, C. Cayron, A.-.M. Lancha, P. Fernández, N. Baluc, R. Schäublin, E. Diegele, G. Filaccioni, J.W. Rensman, B.v.d. Schaaf, E. Lucon, W. Dietz, Present development status of EUROFER and ODS-EUROFER for application in blanket concepts, Fusion Eng. Des. 75-79 (2005) 989–996 https://doi.org/10.1016/j.fusengdes.2005.06.186.

[7] G.R. Odette, M.J. Alinger, B.D. Wirth, Recent developments in irradiation-resistant steels, Annu. Rev. Mater. Res. 38 (2008) 471–503 https://doi.org/10.1146/annurev.matsci.38.060407.130315.

[8] S. Ukai, T. Nishida, T. Okuda, T. Yoshitake, R&D of oxide dispersion strengthened ferritic martensitic steels for FBR, J. Nucl. Mater. 258 (1998) 1745–1749 https://doi.org/10.1016/S0022-3115.

[9] S. Ukai, S. Mizuta, M. Fujiwara, T. Okuda, T. Kobayashi, Development of 9Cr-ODS martensitic steel claddings for fuel pins by means of ferrite to austenite phase transformation, J. Nucl. Sci. Technol. 39 (2002) 778–788 https://doi.org/10.1080/18811248.2002.9715260.

[10] M. Inoue, T. Kaito, S. Ohtsuka, et al., Research and development of oxide dispersion strengthened ferritic steels for sodium cooled fast breeder reactor fuels, in: V. Ghetta, et al. (Ed.), Materials Issues for Generation IV Systems, 2008.

[11] A.L. Rouffié, P. Wident, L. Ziolek, F. Delabrouille, B. Tanguy, J. Crépin, A. Pineau, V. Garat, B. Fournier, Influences of process parameters and microstructure on the fracture mechanisms of ODS steels, J. Nucl. Mater. 433 (2013) 108–115 https://doi.org/10.1016/j.jnucmat.2012.08.050.

[12] S. Ukai, S. Ohtsuka, Nano-mesoscopic structure control in 9Cr–ODS ferritic steels, Energy Mater 2 (1) (2007) 26–35 https://doi.org/10.1179/174892407×210357.

[13] C. Cayron, E. Rath, I. Chu, S. Kaunois, Microstructural evolution of Y_2O_3 and $MgAl_2O_4$ ODS EUROFER steels during their elaboration by mechanical milling and hot isostatic pressing, J. Nucl. Mater. 335 (2004) 83–102 https://doi.org/10.1016/j.jnucmat.2004.06.010.

[14] M. Yamamoto, S. Ukai, S. Hayashi, T. Kaito, S. Ohtsuka, Reverse phase transformation from α to γ in 9Cr-ODS ferritic steels, J. Nucl. Mater. 417 (2011) 237–240 https://doi.org/10.1016/j.jnucmat.2010.12.250.

[15] B. Hary, T. Guilbert, P. Wident, T. Baudin, R. Logé, Y. de Carlan, Investigation of the relationships between mechanical properties and microstructure in a Fe-9%Cr ODS steel, Nucl. Sci. Technol. 2 (7) (2016) 2–8 https://doi.org/10.1051/epjn/e2016-50008-7.

[16] M. Serrano, F. Bergner, U. Ehrnsten, Y. de Carlan, A. Heinzel, A. Weisenburger, Detailed Work Plan and Testing Matrices, (Jul 2014) MatISSE Deliverable D4.11.

[17] E. Vanegas-Márquez, K. Mocellin, L. Toualbi, Y. de Carlan, R.E. Logé, A simple approach for the modeling of an ODS steel mechanical behavior in pilgering conditions, J. Nucl. Mater. 420 (2012) 479–490 https://doi.org/10.1016/j.jnucmat.2011.10.013.

[18] L. Toualbi, C. Cayron, P. Olier, J. Malaplate, M. Praud, M.-.H. Mathon, D. Bossu, E. Rouesne, A. Montani, R. Logé, Y. de Carlan, Assessment of a new fabrication route for Fe–9Cr–1W ODS cladding tubes, J. Nucl. Mater. 428 (2012) 47–53 https://doi.org/10.1016/j.jnucmat.2011.12.013.

[19] S. Lozano-Perez, V. de Castro Bernal, Achieving sub-nanometre particle mapping with energy-filtered TEM, in: R.J. Nicholls (Ed.), Achieving sub-nanometre particle mapping with energy-filtered TEM, Ultramicroscopy 109 (2009) 1217–1228 https://doi.org/10.1016/j.ultramic.2009.05.006.

[20] N. Roduit, JMicroVision, <http://www.jmicrovision.com.

[21] M.H. Loretto, Interpretation of diffraction information, Electron Beam Analysis of Materials, Springer, 1984, https://doi.org/10.1007/978-94-009-5540-0_4.

[22] CEN Workshop agreement, Small punch test method for metallic materials, CWA 15627:2007 D/E/F, December 2007.

[23] M. Serrano, M. Hernández-Mayoral, A. García-Junceda, Microstructural anisotropy effect on the mechanical properties of a 14Cr ODS steel, J. Nucl. Mater. 428 (2012) 103–109 https://doi.org/10.1016/j.jnucmat.2011.08.016.

[24] E.A. Marquis, Core/shell structures of oxygen-rich nanofeatures in oxide-dispersion strengthened Fe–Cr alloys, Appl. Phys. Lett. 93 (2008) 181904https://doi.org/10.1063/1.3000965.

[25] M. Klimenkov, R. Lindau, A. Möslang, New insights into the structure of ODS particles in the ODS-Eurofer alloy, J. Nucl. Mater. 386-388 (2009) 553–556 https://doi.org/10.1016/j.jnucmat.2008.12.174.

[26] J. Ribis, S. Lozano-Perez, Nano-cluster stability following neutron irradiation in MA957 oxide dispersion strengthened material, J. Nucl. Mater. 444 (2014) 314–322 https://doi.org/10.1016/j.jnucmat.2013.10.010.

[27] R.J. Parrington, Fractographic features in metals and plastics, Adv. Mater. Process. 161 (2003) 37–40.

[28] Z. Dapeng, L. Yong, L. Feng, W. Yuren, Z. Liujie, D. Yuhai, ODF ferritic steels engineered with bimodal size for high strength and ductility, Mat. Lett. 65 (2011) 1672–1674 https://doi.org/10.1016/j.matlet.2011.02.064.

[29] H.R.Z. Sandim, R.A. Renzzetti, A.F. Padilha, D. Raabe, M. Klimenkov, R. Lindau, A. Möslang, Annealing behavior of ferritic–martensitic 9%Cr–ODS–Eurofer steel, Mater. Sci. Eng. A 527 (2010) 3602–3608 https://doi.org/10.1016/j.msea.2010.02.051.

[30] S. Ukai, M. Fujiwara, Perspective of ODS alloys application in nuclear environments, J. Nucl. Mater. 307 (2002) 749–757, https://doi.org/10.1016/S0022-3115(02)01043-7.

[31] H. Okada, S. Ukai, M. Inoue, Perspective of ODS alloys application in nuclear environments, J. Nucl. Sci. Tech. 33 (1996) 936–943 https://doi.org/10.1016/S0022-3115.

[32] K. Kaneko, S. Matsumura, A. Sadakata, K. Fujita, W.-.J. Moon, S. Ozaki, N. Nishimura, Y. Tomokiyo, Characterization of carbides at different boundaries of 9Cr-steel, Mater. Sci. Eng. A 374 (2004) 82–89 https://doi.org/10.1016/j.msea.2003.12.065.

[33] H. Sakasegawa, S. Ohtsuka, S. Ukai, H. Tanigawa, M. Fujiwara, H. Ogiwara, A. Kohyama, Particle size effects in mechanically alloyed 9Cr ODS steel powder, J. Nucl. Mater. 367-370 (2007) 185–190 https://doi.org/10.1016/j.jnucmat.2007.03.148.

[34] F. Abe, Precipitate design for creep strengthening of 9% Cr tempered martensitic steel for ultra-supercritical power plants, Sci. Technol. Adv. Mater. 9 (2008) 15 013002 https://stacks.iop.org/STAM/9/013002.

[35] N. Salez, C. Hatzoglou, F. Delabrouille, D. Sornin, L. Chaffron, M. Blat-Yrieix, B. Radiguet, P. Pareige, P. Donnadieu, Y. Bréchet, Precipitates and boundaries interaction in ferritic ODS steels, J. Nucl. Mater. 472 (2016) 118–126 https://doi.org/10.1016/j.jnucmat.2016.01.021.

[36] A. Chauhan, D. Litvinov, Y. de Carlan, J. Aktaa, Study of the deformation and damage mechanisms of a 9Cr-ODS steel: Microstructure evolution and fracture characteristics, Mat. Sci. Eng. A (2016) 123–134 https://doi.org/10.1016/j.msea.2016.01.109.

[37] F. Abe, T. Horiuchi, M. Taneike, K. Sawada, Stabilization of martensitic microstructure in advanced 9Cr steel during creep at high temperature, Mater. Sci. Eng. A 378 (2004) 299–303 https://doi.org/10.1016/j.msea.2003.11.073.

[38] K. Maruyama, K. Sawada, J. Koike, Strengthening mechanisms of creep resistant tempered martensitic steel, ISIJ Int. 41 (2001) 641–653 https://doi.org/10.2355/isijinternational.41.641.

[39] H. Sakasegawa, F. Legendre, L. Boulanger, M. Brocq, L. Chaffron, T. Cozzika, J. Malaplate, J. Henry, Y. de Carlan, Stability of non-stoichiometric clusters in the MA957 ODS ferrtic alloy, J. Nucl. Mater. 417 (2011) 229–232 https://doi.org/10.1016/j.jnucmat.2010.12.056.

[40] J.S. Lee, I.S. Kim, Evaluation of mechanical properties of RPV clad by small punch tests, Nucl. Eng. Technol. 34 (6) (2002) 574–585.

[41] M. Praud, F. Mompiou, J. Malaplate, D. Caillard, J. Garnier, A. Steckmeyer, B. Fournier, Study of the deformation mechanisms in a Fe–14% cr ODS alloy, J. Nucl. Mat. 428 (2012) 90–97 https://doi.org/10.1016/j.jnucmat.2011.10.046.

[42] T.S. Byun, J.H. Kim, J.H. Yoon, D.T. Hoelzer, High temperature fracture characteristics of a nanostructured ferritic alloy (NFA), J. Nucl. Mater. 407 (2010) 78–82 https://doi.org/10.1016/j.jnucmat.2010.09.031.